JTTEE5 11:36-43

Simulation and Application of a HVOF Process for MCrAlY Thermal Spraying

Young-myung Yang, Hanlin Liao, and Christian Coddet

(Submitted 21 June 2000; in revised form 17 January 2001)

This work deals with numerical simulation and application of a high velocity oxygen fuel (HVOF) process for MCrAlY thermal spraying. The main objective of this study was to observe the correlations between coating oxidation and oxygen content in combustion products or flame temperature. Spray parameters were selected on the basis of the numerical simulation of combustion and particle behavior in the flame. The results of experiments revealed that the oxygen content is not the main key factor concerning the oxidation rate of MCrAlY coatings. On the contrary, the flame temperature has a decisive influence on oxidation. Combustion conditions corresponding to stoichiometric factors between 0.82 and 1.2 appeared not to be favorable for MCrAlY thermal spraying. Outside this range, it appeared preferable to use a combustion system on the fuel-rich side.

Keywords coating, combustion, flame temperature, HVOF process, MCrAlY, oxide

1. Introduction

MCrAlY alloys are well known for their excellent resistance to corrosion and oxidation at high temperatures. These alloys were developed mainly by aircraft engine manufacturers to provide a corrosion and oxidation resistance barrier on parts operating in the hot sections of jet engines, and they are usually applied as thermal spray coatings.[1] Thermal spray is usually conducted with Vacuum Plasma Spraying (VPS) or Low Pressure Plasma Spraying (LPPS) processes to avoid oxide forming in the coatings.[2-4] Application of a high velocity oxygen fuel (HVOF) process to MCrAlY spraying already has been studied by several authors, for example Parker and Kutner,[5] Irons and Zanchuk,[6] Nestler et al.,[7] Russo and Dorfman,[8] and Sasaki et al.[9] These studies have reported that a "near-chamber-quality" MCrAlY coating was obtainable using HVOF spraying.

While spraying MCrAlY powders with an HVOF process, an essential problem to be considered is the formation of oxides in the coatings.[10] These oxides can be produced by chemical reactions with oxygen originating either from combustion products or from air entrained from the atmosphere. Oxidation normally is related to particle temperature. Accordingly, the oxygen content in combustion products and the flame temperature both have to be taken into account in choosing spray parameters.

Therefore, this article deals with a numerical simulation of combustion characteristics and particle behavior, and discusses how to choose spray parameters. The correlations between coating characteristics and combustion properties also are reported. Numerical simulations were conducted by using the computation code HVOF-CEP,[11] which had been constructed previously in the Laboratoire d'Etudes et de Recherches sur les Matériaux et les Propriétés de Surface (Belfort, France). Spray parameters were chosen on the basis of the numerical simulation results. Experimental works were conducted with a prototype HVOF torch of the chamber-stabilized type[11] using natural gas as the fuel. Amdry (Sulzer Metco, Troy, MI) 9954 powder (Co-32%Ni-21%Cr-8%Al-0.5%Y) was employed as a coating material. The chemical composition of natural gas used for this study is given in Table 1.

Young-myung Yang, R&D Center, Korea Gas Corporation, 638-1, Il-dong, Ansan, Kyunggi-do, South Korea; and **Hanlin Liao** and **Christian Coddet,** Laboratoire d'Etudes et de Recherches sur les Matériaux et les Propriétés de Surface (LERMPS), Université de Technologie de Belfort-Montbéliard, 90010 Belfort Cedex, France. Contact e-mail: christian.coddet@utbm.fr.

2. Combustion Characteristics

Combustion properties were calculated on the basis of equilibrium chemistry, specifically by using the free energy minimization method.[11] With a natural gas flow rate fixed at 200 standard liters per minute (slm), the following four combustion systems described below were chosen to observe the combustion characteristics of natural gas: system A, natural gas (200) + oxygen (variable); system B, natural gas (200 slm) + oxygen (variable) + air (50 slm); system C, natural gas (200 slm) + oxygen (variable) + air (95 slm); and system D, natural gas (200 slm) + oxygen (variable) + air (145 slm).

The oxygen flow rate was varied according to stoichiometric conditions (factor *St*), i.e., the ratio of the oxygen flow rate over the ideal oxygen flow rate necessary for stoichiometric combustion (*St* = 1). Air was added between 50 and 145 slm in order to allow a larger evolution of the flame temperature. The oxygen content in the added air was taken into account for the determination of the stoichiometric factor.

Table 1 Chemical Composition of Natural Gas Used for Experimental Work

Constituents	mol%	Constituents	mol%
CH_4	95.6706	i-C_5H_{12}	0.0115
C_2H_6	1.4346	n-C_5H_{12}	0.0095
C_3H_8	0.3268	C_6H_{14}	0.0114
i-C_4H_{10}	0.0424	CO_2	0.2636
n-C_4H_{10}	0.0561	N_2	2.1717

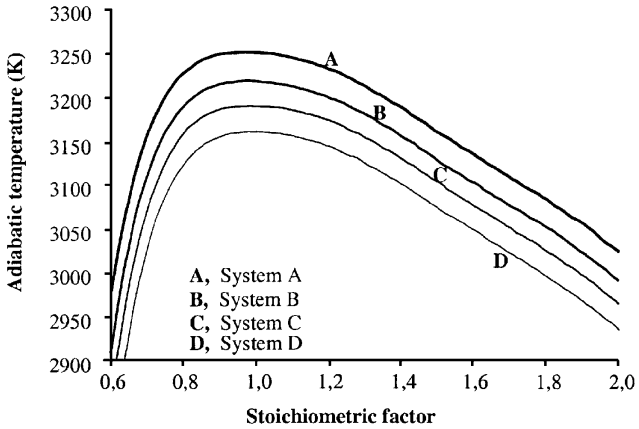

Fig. 1 Theoretical adiabatic flame temperatures for different combustion systems at 5 bars (absolute pressure)

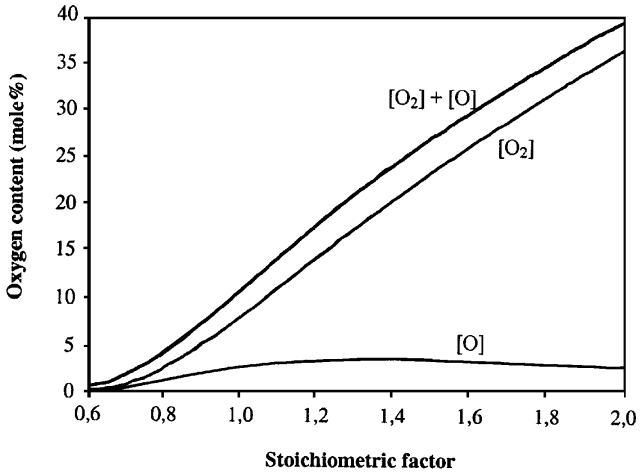

Fig. 2 Evolution of the oxygen content in the combustion products vs the stoichiometric condition for system A at 5 bars (absolute pressure)

Table 2 Spray Parameters and Calculated Combustion Characteristics (a)

Spray Parameters	NG, slm	Oxygen, slm	Air, slm	*St*	Tad, K	O_2, mol%	O, mol%	$[O_2] + [O]$ mol%
P1	200	260	145	0.725	3076	0.70	0	0.70
P2	200	280	145	0.781	3114	1.25	0.7	1.95
P3	200	300	95	0.805	3155	1.90	1.03	2.93
P4	200	340	95	0.905	3187	4.10	1.67	5.77
P5	190	360	95	1.005	3190	6.70	2.14	8.84
P6	190	400	95	1.111	3181	9.71	2.51	12.22
P7	180	420	95	1.228	3159	13.08	2.72	15.80
P8	170	440	95	1.340	3128	16.80	2.79	19.59
P9	160	460	95	1.507	3089	20.84	2.75	23.59
P10	200	380	50	0.982	3225	6.63	2.33	8.96
P11	200	400	0	1.005	3253	8.11	2.84	11.95
P12	200	400	50	1.032	3219	8.08	2.57	10.65

(a) NG—natural gas; Tad—adiabatic flame temperature; O_2—molecular oxygen content in mol% in the combustion products; O—atomic oxygen content in mol% in the combustion products.

Figure 1 shows the adiabatic flame temperature evolution as a function of the stoichiometric condition for the four combustion systems. The adiabatic flame temperature reaches a peak close to the stoichiometric combustion temperature on the slightly fuel-rich side ($St < 1$). It was also observed that an additional gas (i.e., air or nitrogen) is more efficient in decreasing flame temperature on the fuel-rich side.

Figure 2 shows the atomic and molecular oxygen content evolutions in the combustion products for combustion system A. In the case of fuel-lean combustions ($St > 1$), oxygen content increases naturally with the increase of the stoichiometric factor. But even in a far fuel-rich condition, it is not possible to completely eliminate the oxygen in the flame because of the chemical equilibrium. Figure 2 indicates that an atomic oxygen content of 3% and a molecular oxygen content of 8% are to be expected in the combustion products for the stoichiometric combustion.

From the above observations, it appears necessary to select the combustion system on the far fuel-rich side to reduce both flame temperature and oxygen content in combustion products. But it should also be noted that the flame temperature must be high enough to melt particles. Besides, these calculations do not take into account a further evolution of the oxygen content around the particles that is the result of the entrainment of the surrounding atmosphere.

3. Spray Parameters

Supposing that the influence of entrained air from the atmosphere into the free jet would not vary too much with the different spray parameters and taking into account the combustion characteristics shown in Fig. 1 and 2, 12 sets of spray parameters (P1 to P12) were chosen with different oxygen contents. Table 2 presents the selected spray parameters and the corresponding combustion properties. Spray parameters P1 to P4 are on the fuel-rich side, P6 to P9 are on the fuel-lean side, and P5 and P10 to P12 are close to the stoichiometry. As shown in Fig. 3, the parameters of P1 to P9 correspond to a linear evolution of the oxygen content in the flame and to a parabolic evolution of the adiabatic flame temperature versus the stoichiometric factor. Parameters P10 to P12 were chosen in order to observe the influ-

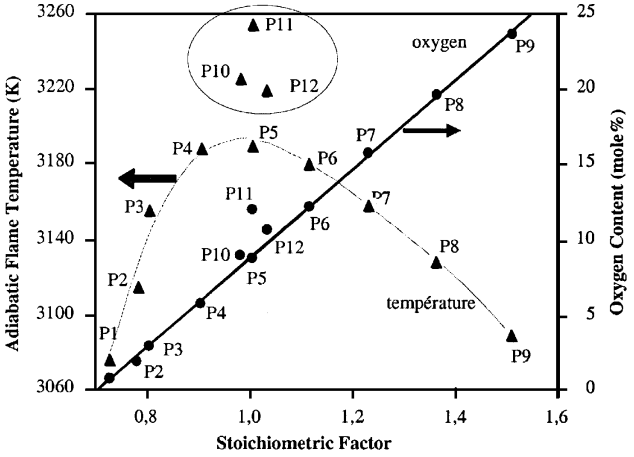

Fig. 3 Adiabatic flame temperatures and oxygen contents for various spray parameters selected for CoNiCrAlY spraying experiments

Table 3 Physicochemical Properties of the CoNiCrAlY Powder Used for the Numerical Calculations

Properties	Values	Remarks
Chemical composition	Co-32%Ni-21%Cr-8% Al-0.5%Y	Amdry 9954
Density at 300 K	7992 kg/m^3	Mixing rule used
Specific heat at 300 K	473 J/kg/K	Mixing rule used
Latent heat of fusion	293.7 kJ/kg	Mixing rule used
Thermal conductivity	2.5-5.5 W/m/K	Ref 12
Melting point	1653 K	Binary-phase diagrams

ence of the flame temperature on the coating characteristics. Experimental results for these three parameters will have to be compared with those obtained for parameter P5.

4. Numerical Simulation of MCrAlY Particle Behavior

Among the 12 sets of spray parameters indicated in Table 2, the P8 set was selected in order to observe the thermal and dynamic behavior of CoNiCrAlY particles. The physicochemical properties of this material that were used for the numerical simulation are indicated in Table 3. The density, specific heat, and latent heat of fusion of the particles were calculated using mixing rules. The density and the specific heat of each element were expressed as a function of temperature as described below.

- Density for the element *j*:

$$\rho_j = \rho_o(a_1 + a_2 10^{-5} T + a_3 10^{-9} T^2) \quad \text{for the solid phase}$$
$$\rho_j = \rho_m - \beta(T - T_m) \quad \text{for the liquid phase}$$

- Specific heat for the element *j*:

$$C_{pj} = c_1 + c_2 10^{-3} T + c_3 10^{-6} T^2 + c_4 10^{-5} T^2$$

where ρ_o and ρ_m are, respectively, the densities of the element *j* at 0 °C and at its melting point (T_m). The coefficients a_1 to a_3, b, and c_1 to c_4 for each element are available in Ref 12-14. In most cases, the application of mixing rules to thermal conductivity calculations results in a large error.

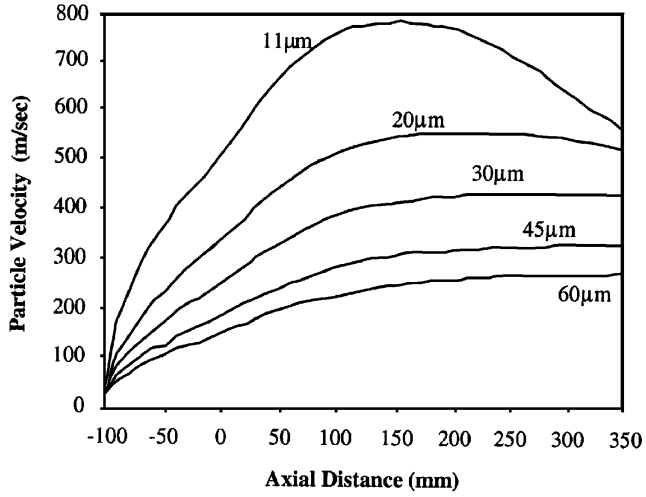

Fig. 4 CoNiCrAlY particles velocity profiles calculated for the spray parameters P8 (the location indicates the nozzle exit position)

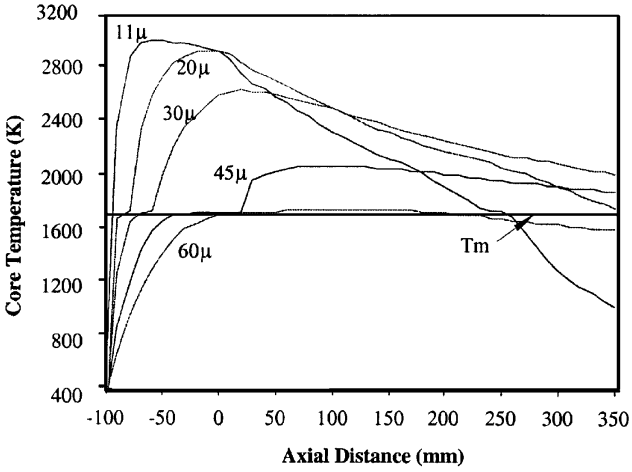

Fig. 5 Core temperature evolutions of different-sized CoNiCrAlY particles (spray parameters P8)

Therefore, we used experimental data taken from the works of Holmes and McKechnie[15] on Atmospheric Plasma Spraying (APS) sprayed NiCrAlY coatings (since no experimental data was available for CoNiCrAlY alloys). The melting point was deduced from the binary phase diagrams of Co-Ni, Co-Cr, and Ni-Cr.

Velocity profiles calculated for various particle sizes are shown in Fig. 4. For particles smaller than 30 µm, the maximum velocity is obtained at a distance of less than 300 mm from the nozzle exit. For example, the velocity reaches a maximum value at a distance of 150 mm for an 11 µm particle and at a distance of 220 mm for a 20 µm particle. Figure 5 shows the temperature evolution in the core of the particles versus the distance from the nozzle exit. In this figure, flat parts correspond to the melting point and result from the high latent heat of fusion of the CoNiCrAlY alloy. A flat section also is found in the resolidification process, which, for the smaller particles, starts not very far from nozzle exit. The 11 µm particles appear to be entirely resolidified at the distance of 250 mm and then rapidly cool down to a tem-

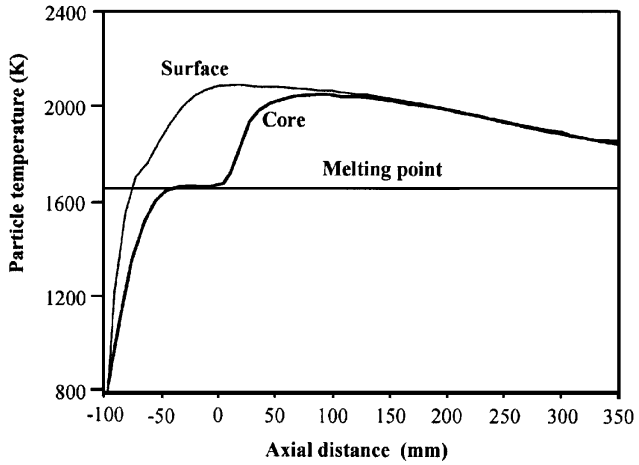

Fig. 6 Surface and core temperature profiles of a 45 μm CoNiCrAlY particle (calculated for the parameters P8)

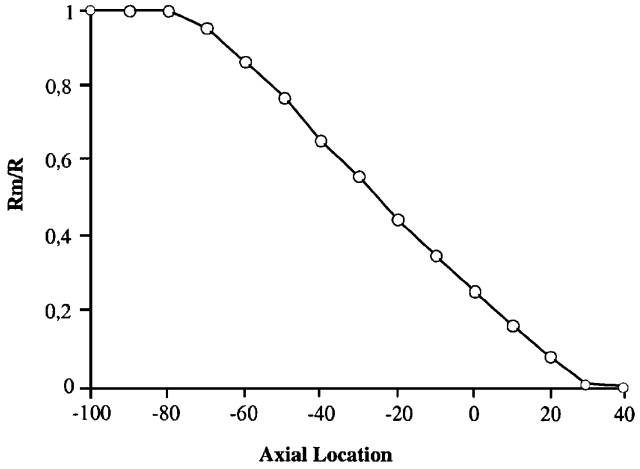

Fig. 7 Melting front evolution inside a 45 μm diameter CoNiCrAlY particle (calculated for the P8 set of parameters; 0 = nozzle exit). Rm/R = the proportion of the radius of the particle which is melted (Rm) over the radius of the particle (R).

perature 430 °C below the melting point at the distance of 300 mm. The 60 μm particles begin to be molten at the position of −50 mm inside the torch nozzle, and the melting front moves to half of the radius (15 μm) at the distance of 130 mm from the nozzle exit. From this position, this partially molten particle resolidifies progressively and becomes completely solid at a distance of 170 mm. At a distance of 300 mm, the core temperature of this particle is about 100 °C below its melting point.

Figure 6 shows the core and surface temperature profiles, and Fig. 7 shows the melting front evolution for a 45 μm CoNiCrAlY particle (again, for the P8 set of spraying parameters). This particle begins to melt at the position of −80 mm inside the torch nozzle and is completely molten at a distance of 30 mm. The maximum difference reached between the core and the surface temperatures is approximately 400 °C.

When a standoff distance is chosen, it is then necessary to observe particle velocity and temperature as a function of particle size at this standoff distance. Figure 8 presents velocity and core temperature profiles of particles for a standoff distance of 300 mm. The particle velocity decreases with an increase in the particle size, while the core temperature goes through a maximum value for a 30 μm particle and then decreases. This figure indicates that particles smaller than 15 μm and larger than 57 μm are not likely to contribute to the coating formation.

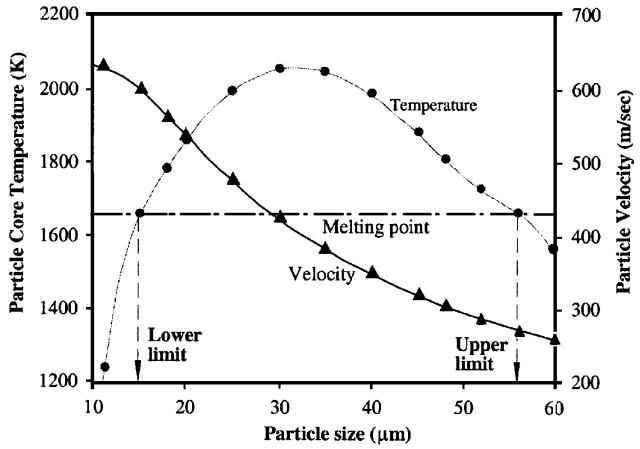

Fig. 8 Evolution of particles velocity and core temperature as a function of the particle size at the standoff distance of 300 mm

5. Experiments and Results

Experiments were carried out with the 12 sets of spray parameters given in Table 2. The spray distance of 300 mm was selected by considering the particle velocity and temperature profiles shown in Fig. 4 and 5.

A stainless steel (316) coupon of dimensions 27 × 80 × 3 mm^3 were used for metallographic analyses and microhardness tests. These coupons were chemically cleaned and then grit blasted with 500 μm white alumina grits. After grit blasting, the coupons were weighed before being fixed at the periphery of a 100 mm diameter cylindrical holder. During spraying, the drum was rotated at 250 rotations per minute (RPM) and the torch was moved with a linear velocity of 40 mm/s parallel to the drum axis. Air cooling using air jets was applied to the specimens.

Sprayed coupons then were weighed again to determine the deposition efficiency, and then the coatings were characterized for surface roughness (*Ra*), porosity, microhardness, oxide content, and unmelted particle content. Roughness measurements were carried out using a Surtronic 3P (Taylor-Hobson, Villebon sur Yvette, France) apparatus, and the microhardness was measured under a 300 g (2.942 N) load with a Leitz Miniload 2 Vickers microhardness tester (LEICA, Lyon, France). The rates of porosity for the oxides and unmelted particles were estimated by image analysis on polished cross-sections.

Table 4 presents the coating characteristics for the given spray parameters. One may observe that porosity values remain lower than 1% for all of the coatings. On the contrary, the microhardness and the deposition efficiency vary by 30% depending on the spray parameters. Above all, the rate of oxides and unmelted particles vary still more drastically. The correlations observed between these coatings characteristics and the combustion properties are described in the following sections.

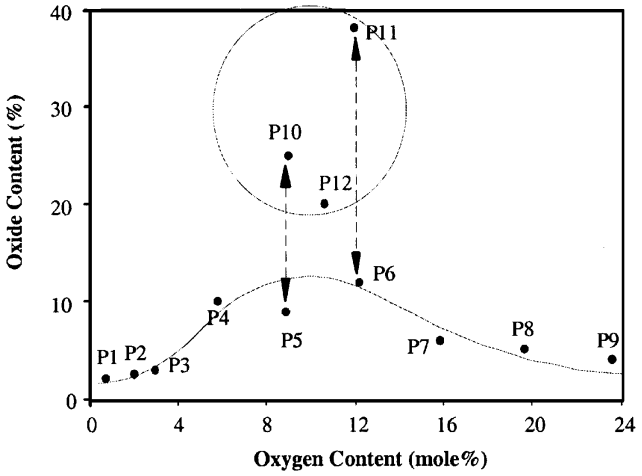

Fig. 9 Oxide content of the coatings vs oxygen content in the combustion products

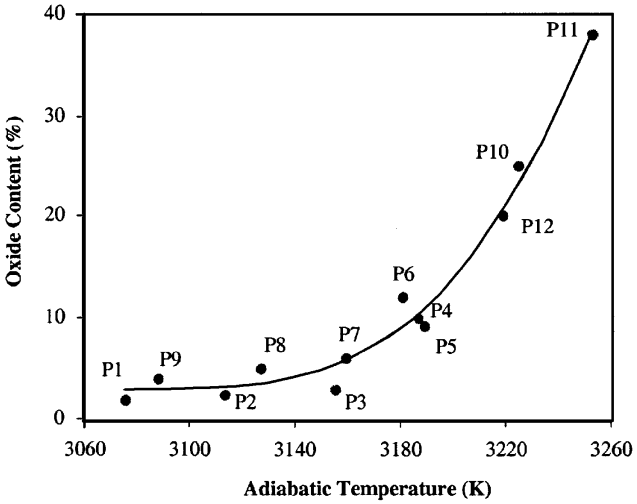

Fig. 10 Oxide content of the coatings vs the adiabatic flame temperature

Table 4 Characteristics of CoNiCrAlY Coatings Obtained with the Spray Parameters Given in Table 2(a)

Spray Parameters	Ra, μm	Porosity, %	HV300	Oxides, %	Unmelted, %	η, %
P1	7.1 ± 0.7	0.2	487 ± 34	2 ± 0.5	5 ± 0.5	68.4
P2	7.2 ± 0.7	0.3	462 ± 47	3 ± 0.5	4 ± 0.5	62.7
P3	7.6 ± 0.8	0.2	484 ± 45	3 ± 0.5	3 ± 0.5	61.2
P4	7.4 ± 0.7	0.2	472 ± 46	10 ± 1	2 ± 0.5	55.2
P5	7.3 ± 0.7	0.2	470 ± 50	9 ± 1	1 ± 0.2	56.5
P6	6.9 ± 0.7	0.3	476 ± 42	12 ± 2	2 ± 0.5	57.8
P7	6.8 ± 0.6	0.4	438 ± 26	6 ± 1	10 ± 1	62.7
P8	7.3 ± 0.7	0.6	422 ± 39	5 ± 0.5	15 ± 1	64.7
P9	7.7 ± 0.7	0.6	393 ± 54	4 ± 0.5	23 ± 2	66.2
P10	6.0 ± 0.7	0.2	505 ± 34	25 ± 2	0	54.3
P11	5.9 ± 0.8	0.1	517 ± 31	38 ± 3	0	52.6
P12	6.2 ± 0.6	0.6	497 ± 28	20 ± 2	0	55.6

(a) HV300—Vickers microhardness under a load of 300 g; Oxides—oxide content in coating (% area from image analysis); Unmelted—unmelted particle content (% area from image analysis); η—deposition efficiency. Values given as mean ± SD, unless otherwise indicated.

5.1 Oxidation of Coatings

As indicated previously, the sets of parameters P1 to P9 correspond to a linear relationship between the oxygen content in the combustion products and the stoichiometric factor, as shown in Fig. 3. The sets P10 to P12 have oxygen levels that are nearly identical to that of the P5 set, but the adiabatic flame temperature is much higher.

Figure 9 shows the evolution of the oxide content in the coatings with the oxygen content in the combustion products. The oxide content increases with the oxygen content for the sets of parameters P1 to P4 on the fuel-rich side. But for the P6 to P9 sets, which are on the fuel-lean side, the oxide content decreases as the oxygen content increases, even though the oxygen content increases quite significantly. The three sets P10 to P12 provide much higher oxide contents than the set P5 for very similar oxygen contents in the flame. This clearly means that the oxygen content in the combustion products is not the main key factor for the coating oxidation.

Figure 10 presents the oxide content evolution in the coatings as a function of the adiabatic flame temperature. Here the oxide content appears to increase with the adiabatic flame temperature in a nearly exponential manner. Meanwhile, at the same adiabatic flame temperature, a fuel-lean combustion gives an oxide content that is slightly higher in the fuel-rich combustion (see, for example, P6/P4 or P7/P3).

From the above observations, it can be concluded that the coating oxidation only slightly depends on the oxygen content in the combustion products, whereas it depends very strongly on the flame temperature. It seems then, accordingly, to be preferable to take a combustion system on the far fuel-rich side ($St < 0.82$) and to limit the adiabatic flame temperature at about 3160 °C.

5.2 Unmelted Particles

The variation of the unmelted particle rate in the coatings as a function of the adiabatic flame temperature is shown in Fig. 11. It is easy to observe that, for an identical flame temperature, when the temperature is relatively low (i.e., lower than 3180 °C), the parameters on the fuel-rich side provide an unmelted particle rate that is much lower than those on the fuel-lean side. This fact is probably related to the thermal conductivity difference,

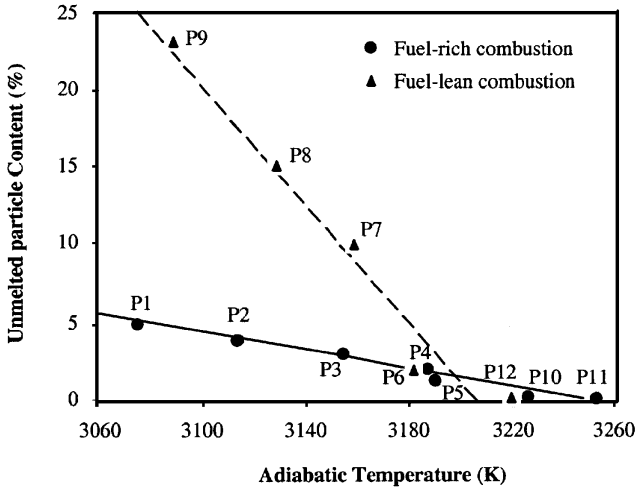

Fig. 11 Unmelted particle content of the coatings as a function of the adiabatic flame temperature

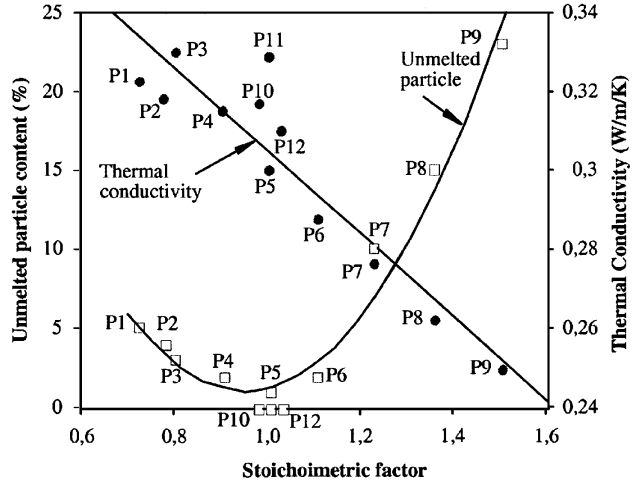

Fig. 12 Thermal conductivity of the combution products and unmelted particles content of the coatings as a function of the stoichiometric factor

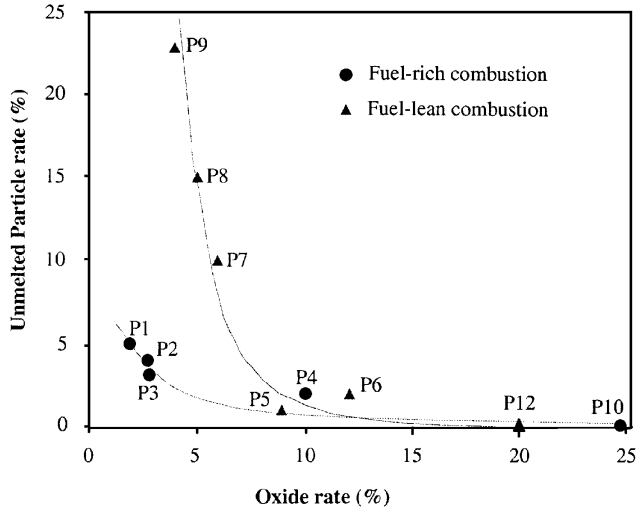

Fig. 13 Correlation between the unmelted particle rate and the oxide rate in the coatings

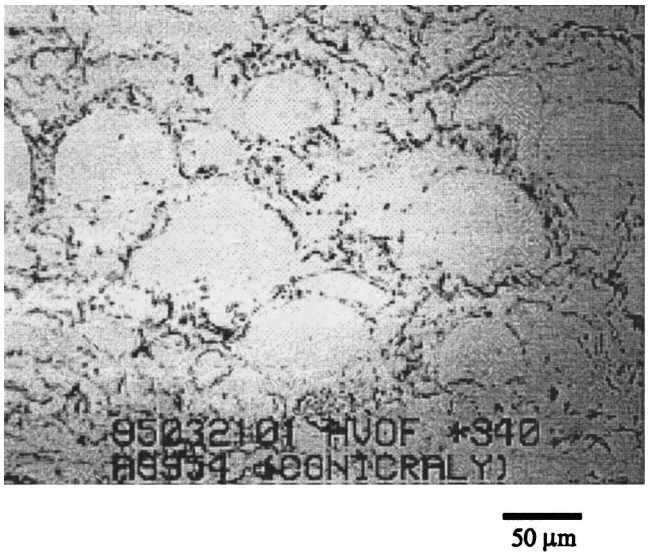

Fig. 14 Cross-sectional microstructure of a CoNiCrAlY coating sprayed using the P8 set of spraying parameters

as shown in Fig. 12. The unmelted particle rate increases very rapidly on the fuel-lean side as the thermal conductivity of the flame decreases. A fuel-rich combustion provides more light species such as H and H2 than does a fuel-lean combustion.

Figure 13 shows the existence of a good correlation between the oxide rate and the unmelted particle rate. The two move in opposite directions. Here again, the profile for the fuel-rich combustion side is much different from that for the fuel-lean combustion side. For the same oxide content, the fuel-lean combustion provides an unmelted particle rate that is much higher than that of the fuel-rich combustion, probably due to the lower thermal conductivity of the combustion products.

Moreover, in section 4 above, the calculations conducted for the P8 set of spray parameters showed that particles larger than 57 µm would not be entirely melted. It can be observed, from Fig. 14, that the sizes of the unmelted particles are found in the coating range of 50 to 60 µm. This argument seems to give some more confidence that the numerical simulation using the computation code HVOF-CEP can provide a reasonable estimation of the particle behavior in an HVOF flame field.

5.3 Microhardness

Figures 15 and 16 show, respectively, the evolutions of microhardness and the unmelted particle rate with the oxide rate in the coatings. Microhardness increases slightly as the oxide content increases, while it decreases significantly as the unmelted particle content increases. The bulk CoNiCrAlY coatings consist normally of a two-phase mixture of β-(Co,Ni)Al and γ-(Co,Ni), which is fine and randomly oriented. The random grain orientation between the β and γ phases means that the mi-

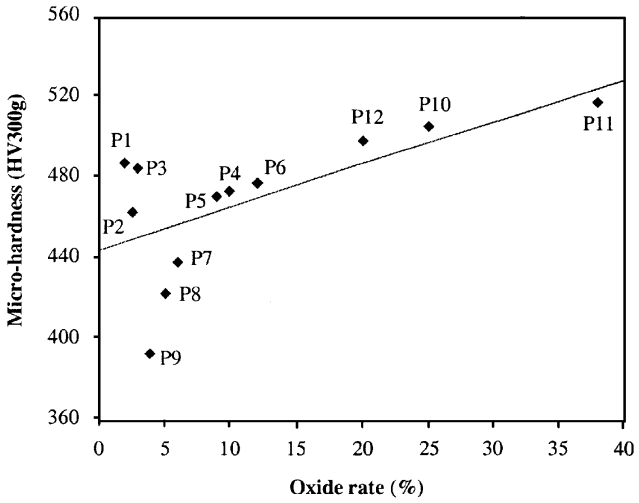

Fig. 15 Correlation between the microhardness and the oxide rate in the coatings. HV = Vickers microhardness.

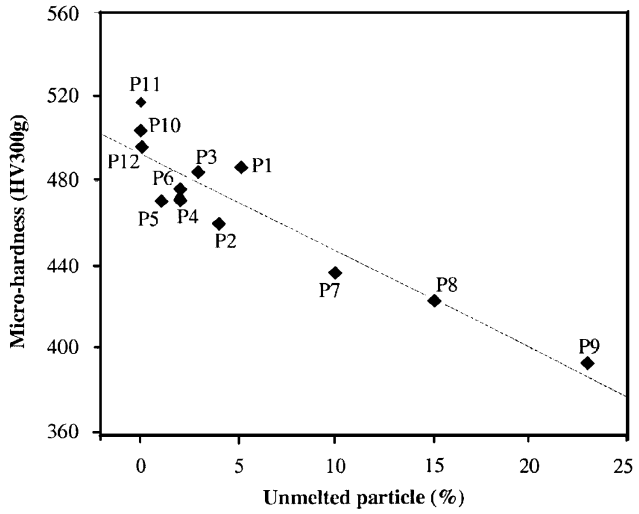

Fig. 16 Correlation between the microhardness and the unmelted particle rate in the coatings. HV = Vickers microhardness.

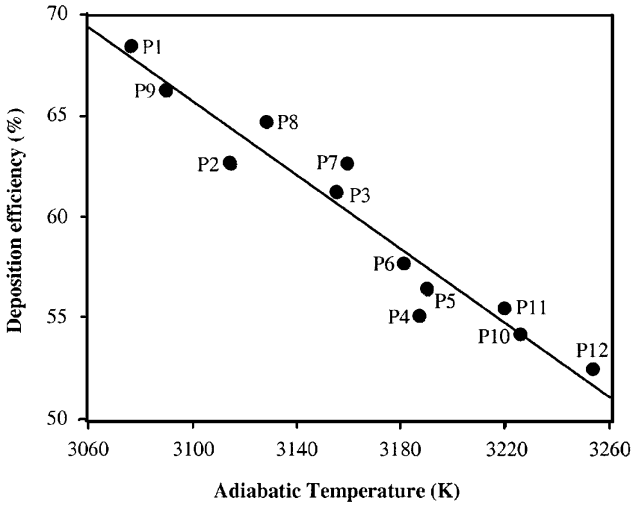

Fig. 17 Evolution of the deposition efficiency vs the adiabatic flame temperature

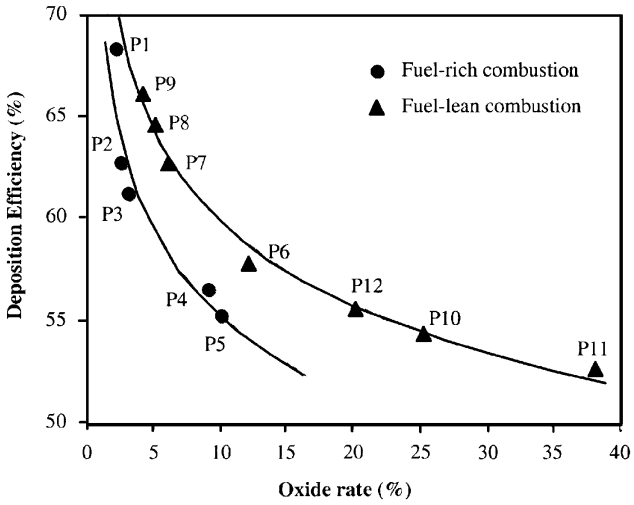

Fig. 18 Correlations between the deposition efficiency and the oxide rate in the coatings

crostructure evolved during the solidification of the coating.[16] Therefore, the presence of unmelted particles provokes a nonhomogeneous microstructure with less β-phase and then a reduction in hardness.

5.4 Deposition Efficiency

Surprisingly, Fig. 17 clearly shows that the deposition efficiency decreases as the adiabatic flame temperature increases. It seems that a higher flame (or particle) temperature produces a more important splashing of the melted particles, which would lower the deposition efficiency. The correlations between, respectively, the oxide rate and the unmelted particle rate and deposition efficiency are shown in Fig. 18 and 19. The deposition efficiency decreases as the oxide content increases, whereas the deposition efficiency increases as the unmelted particle content increases. Again, the evolution profiles for the fuel-rich side are quite different from those for the fuel-lean side. For similar oxide contents, the parameters on the fuel-lean side provide deposition efficiencies that are higher than that on the fuel-rich side.

6. Conclusions

The main objective of this study was to observe the correlations between the rate of oxidation of MCrAlY coatings and both the oxygen content in combustion products and the flame temperature. A series of spraying experiments were conducted with different spray parameters determined on the basis of a numerical computation of combustion characteristics and particles behavior. The results of numerical simulation and the experiments revealed the following:

1) The oxygen content in combustion products is not a key factor governing the oxidation rate of MCrAlY coatings

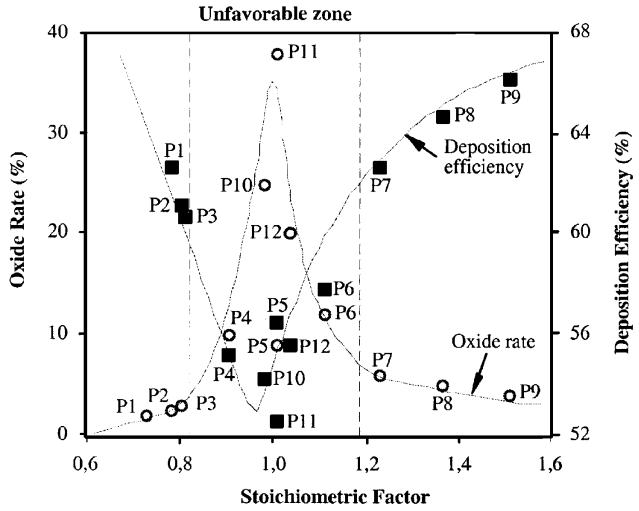

Fig. 19 Correlations between the deposition efficiency and the unmelted particle rate in the coatings

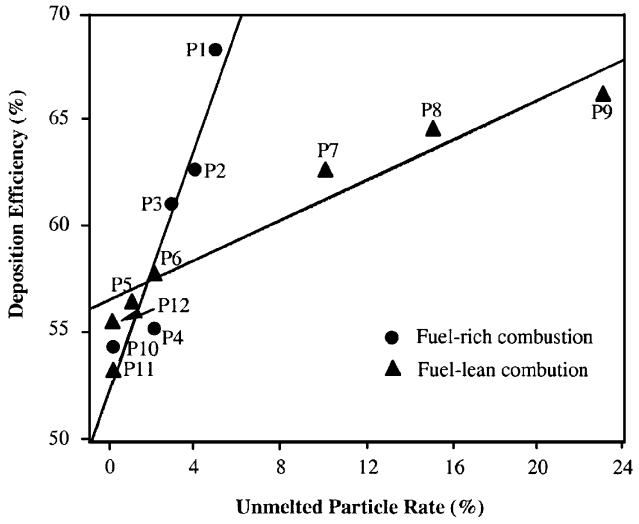

Fig. 20 Oxide content and deposition efficiency of the CoNiCrAlY coatings as a function of the stoichiometric factor

during HVOF spraying. As the oxygen content increases, the oxide content in the coatings increases for fuel-rich combustions but decreases for fuel-lean combustions.

2) The adiabatic flame temperature has, on the contrary, a decisive influence on the oxidation rate of coatings. In order to reduce oxidation, it is necessary to reduce the adiabatic flame temperature to a value lower than approximately 3160 °C (for the present material).
3) The microhardness of coatings decreases significantly as the rate of unmelted particles in the coatings increases.
4) The deposition efficiency decreases as the flame temperature and oxide content increase, while deposition efficiency increases as the unmelted particle rate increases.

Moreover, Fig. 20, displaying the evolutions of the oxide rate and that of the deposition efficiency versus the stoichiometric factor, allows these conclusions:

- Stoichiometric conditions giving a factor comprised between 0.82 and 1.2 are not favorable for the spraying of MCrAlY type powders since the oxide content in coatings is high and the deposition efficiency is relatively low.
- It is preferable to select a combustion system on the far fuel-rich side in order to reduce to the minimum the influence of oxygen and to obtain more easily the flame temperature necessary to correctly melt the particles.

References

1. J.R. Raiden, M.R. Jackson, and M.F.Henry: "The Effects of Low-Pressure Plasma Spray Processing Conditions on the Properties of a Nickel-Based Superalloy," in *Proc. 10th Int. Thermal Spray Conf.*, DVS Deutsche Verband fur Schweisstechnik e.V, Dusseldorf, ed., Essen, Germany, May 2-6, 1983, pp. 205-14.
2. R.M. German: *Powder Metallurgy Science*, Metal Powder Industries Federation, Princeton, NJ, 1984.
3. R. Mevrel and C. Duret: "Interdiffusion, Effects between Protective Coatings on Superalloy Substrates," *Proc. NATO Advanced Workshop: Coatings for Heat Engines*, Aquafredda di Maretea, Italy, April 1-6, 1984, T.P. No.98-11, ONERA, Châtillon, France, 1984.
4. M. Frances, P. Steinmetz, J. Steinmetz, C. Duret, and R. Mevrel: "Hot Corrosion Behaviour of Low Pressure Plasma Sprayed NiCoCrAlY+Ta Coatings on Nickel-Base Superalloys," *Proc. ICMC Congress*, Los Angeles, CA, April 15-19, 1985, T.P. No.985-34, ONERA, Châtillon, France, 1985.
5. D.W. Parker and G.L. Kutner: "HVOF moves into the Industrial Mainstream," *Adv. Mater. Processes*, 1991, *4,* pp. 31-35.
6. G. Irons and V. Zanchuk: "Comparison of MCrAlY Coatings Sprayed by HVOF and Low Pressure Processes," in *Thermal Spray Coatings: Research, Design and Applications*, C.C. Berndt and T.F. Bernecki, ed., ASM International, Materials Park, OH, 1993, pp. 191-97.
7. M.C. Nestler, H.M. Hohle, W.M. Balbach, and T. Koromzay: "Economical Advantages of HVOF Sprayed Coatings for the Land Based Gas Turbine Industry," in *Thermal Spraying: Current Status and Future Trends*, A. Ohmori, ed., High Temperature Society of Japan, Osaka, Japan, 1995, pp. 101-06.
8. L. Russo and M. Dorfman: "High Temperature Oxidation of MCrAlY Coatings Produced by HVOF," in *Thermal Spraying: Current Status and Future Trends*, A.Ohmori, ed., High Temperature Society of Japan, Osaka, Japan, 1995, pp. 1179-84.
9. K. Sasaki, Y. Shimizu, Y. Gouga, and A. Devasenapathi: "Effect of Gun Nozzle Geometry on High Velocity Oxygen-Fuel (HVOF) Thermal Spraying Process," *Thermal Spray: Meeting the Challenges of the 21st Century*, C. Coddet, ed., ASM International, Materials Park, OH, 1998, pp. 445-50.
10. L.B. Temples, M.F. Grununger, and C.H. Londry: "Influence of Oxygen Content on MCrAlYs," in *Thermal Spray Coatings: Research, Design and Applications*, C.C. Berndt and T.F. Bernecki, ed., ASM International, Materials Park, OH, 1993, pp. 359-63.
11. Y.M.Yang: "Modélisation Mathématique d'un Système de Projection Thermique à la Flamme de Type HVOF: Application à l'Elaboration des Revêtements Protecteurs," Ph.D. Thesis, Institut Polytechnique de Sévenans, Belfort, France, July 1996 (in French).
12. W.M. Rohsenow, J.P. Hartnett, and E.N. Ganic: *Handbook of Heat Transfer Fundamentals*, 2nd ed., McGraw-Hill, New York, 1985.
13. R.C. Weast and D.R. Lide: *Handbook of Chemistry and Physics*, 70th ed., CRC Press, Boca Raton, FL, 1989.
14. O. Kubaschewski, C.B. Alcock, and P.J. Spencer: *Materials Thermochemistry*, 6th ed., Pergamon Press, Oxford, England, 1993.
15. R.R. Holmes and T.N. McKechnie: "Vacuum Application of Thermal Barrier Plasma Coatings," *Proc. 1988 Conf. Earth-to-Orbit Propulsion Technol.*, May 10-12, 1988, University of Alabama, Huntsville, AL, 1988.
16. T.C. Totemeier, W.F. Gale, and J.E. King: "Microstructural Changes in MCrAlY Coatings on Nickel-Base Superalloy Single Crystals," *Proc. TS93 Thermal Spraying Conf.*, Aachen, Germany, March 3-5, 1993, DVS 152, pp. 304-06.